Cancer Nanotechnology

RESEARCH Open Access

# Enhanced cancer immunotherapy through synergistic ferroptosis and immune checkpoint blockade using cell membrane-coated nanoparticles

Yeteng Mu[1,2†], Yuxin Fan[2,3†], Lianping He[3†], Nannan Hu[2,3], Han Xue[2,3], Xingang Guan[3*] and Zhijian Zheng[1*]

†Yeteng Mu, Yuxin Fan and Lianping He have contributed equally to this work.

*Correspondence: guanxg@ciac.ac.cn; Zhengzhijian111@163.com

[1] Department of General Surgery, The Affiliated Wenling Hospital of Taizhou University, 333 South Chuanan Road, Taizhou 317500, Zhejiang, People's Republic of China
[2] College of Medical Technology, Beihua University, 3999 East Binjiang Road, Jilin 132013, Jilin, People's Republic of China
[3] Medical School, Taizhou University, 1139 Shifu Avenue, Taizhou 318000, Zhejiang, People's Republic of China

## Abstract

**Background:** Immune checkpoint blockade (ICB) has achieved unprecedented success in inhibiting the progression and metastasis of many cancers. However, ICB regents as a single treatment have a relatively low overall response rate due to the tumor's low immunogenicity and immunosuppressive microenvironment. Herein, we report a PD-1 cellular membrane-coated ferroptosis nanoinducer to potentiate cancer immunotherapy toward triple-negative breast cancer.

**Results:** This study demonstrates that PD-1 membrane-coated RSL3 nanoparticles (PD-1@RSL3 NPs) have the ability to disrupt the PD-1/PD-L1 axis, leading to the activation of antitumor immunity in breast cancer. In addition, the nanoparticles promote the induction of tumor cell ferroptosis through GPX4 inhibition, enhanced infiltration of $CD8^+$ T cells, and maturation of dendritic cells. The potentiated antitumor immune response induced by PD-1@RSL3 NPs significantly delayed tumor progression and extended the survival rate of mice with breast cancer xenografts.

**Conclusions:** Our study suggest the potential of PD-1@RSL3 NPs as an effective therapeutic approach for breast cancer by promoting tumor cell ferroptosis and inducing antitumor immunity.

**Keywords:** Ferroptosis, Drug delivery, PD-1, Cell membrane, Cancer immunotherapy

## Background

Cancer immunotherapy has succeeded in improving the antitumor efficacy of many advanced cancers during the past decade (Waldman et al. 2020; Martin et al. 2020). In particular, immune checkpoint blockade (ICB) has shown promising potential in tumor remission and metastasis inhibition (Robert 2020; Wang et al. 2023). A growing list of antibodies targeting cytotoxic T lymphocyte-associated protein 4 (CTLA-4), programmed cell death protein 1 (PD-1), and programmed death ligand 1 (PD-L1) have been approved to treat cancers (Singh et al. 2020). Despite their clinical success in eradicating tumors, only a subset of cancer patients benefit from the ICB treatment due to the

low immunogenicity and immunosuppressive microenvironment (Carlino et al. 2021; Schoenfeld and Hellmann 2020). ICB-based strategies with high overall response rates remain a significant challenge for improving the outcome of cancer immunotherapy.

Ferroptosis is a unique type of programmed cell death discovered by Dixon et al. in 2012 (Dixon et al. 2012; Liang et al. 2019). Ferroptosis, distinctly different from the reported apoptosis and necrosis, is characterized by overwhelmed lipid peroxidation with ruptured cell membranes (Ye et al. 2020; Li et al. 2020; Hassannia et al. 2019). Ferroptosis can be driven by overloaded iron, reactive oxygen species (ROS) accumulation, and compromised antioxidative defense function (Tang et al. 2021; Jiang et al. 2021; Chen et al. 2021). Some tumors, especially triple-negative breast cancer (TNBC), have evolved to resist tumor ferroptosis by enhanced oxidized phosphatidylethanolamines and glutathione metabolism (Yang et al. 2023, 2022). For example, the antioxidant enzyme glutathione peroxidase 4 (GPX4), which was upregulated in many TNBC patients, prevents ferroptosis by reducing the depletion of phospholipid hydroperoxide (Yang et al. 2014; Xu et al. 2021; Zhang et al. 2020). Recent reports demonstrate that high GPX4 expression is closely related to the poor prognosis of TNBC, and GPX4 inhibition could boost the ferroptosis of tumor cells and trigger the antitumor immune response (Yang et al. 2023).

Promoting ferroptosis provides a novel therapeutic opportunity for improving cancer treatment (Wang et al. 2022a, 2019; Zhou et al. 2022; Xue et al. 2022a; Shi et al. 2021). The ferroptosis of tumors can release damage-associated molecular patterns (DAMPs) or cellular metabolites to activate antitumor immunity, showing a type of immunogenic cell death (ICD) (Wang et al. 2022b). Interestingly, a recent study indicated that the activated $CD8^+$ T cells promoted ferroptotic cell death through GPX4 inhibition (Zhao et al. 2022). Enhanced ferroptosis and ICB collaboratively contribute to the increased ratio of tumor-infiltrating T lymphocytes, ultimately leading to improved efficacy of immunotherapy (Yang et al. 2023; Zhang et al. 2023). Therefore, the positive feedback between tumor cell ferroptosis and ICB holds great promise for effectively eradicating advanced tumors (Liao et al. 2022; Friedmann Angeli et al. 2022). Recent studies have validated the synergistic antitumor effect of tumor ferroptosis and PD-L1 blockade in melanoma and colorectal cancer (Ubellacker et al. 2020; Song et al. 2021). However, their poor solubility and severe toxicities greatly limit the application of ferroptosis inducers in treating cancers (Yan et al. 2022). Suitable vectors for codelivery ferroptosis inducers and ICB reagents are highly desirable for improved safety and antitumor efficacy (Li et al. 2022; Fang et al. 2023).

Cell membrane-based nanovesicles have demonstrated unique advantages in immune regulation for cancer therapy (Meng et al. 2021; Xue et al. 2022b; Ren et al. 2021; Rao et al. 2020). Engineered cell membrane nanovesicles can display immune checkpoint receptors on the surface and selectively bind with their ligands. Therefore, the nanovesicles can disrupt the inhibitory signal pathway (such as PD-L1/PD-1 axis) and revive the exhausted immune cells for immunotherapy (Zhang et al. 2018; Yang et al. 2021; Wang et al. 2021). In this study, we fabricated PD-1 cellular membrane-based nanoparticles (PD-1@RSL3 NPs) for delivering ferroptosis inducer to treat triple-negative breast cancer (TNBC) (Scheme 1). RSL-3, a widely used ferroptosis inducer that inhibits GPX4 activity (Miotto et al. 2020), was encapsulated by DSPE-PEG2000, and the RSL3-loaded

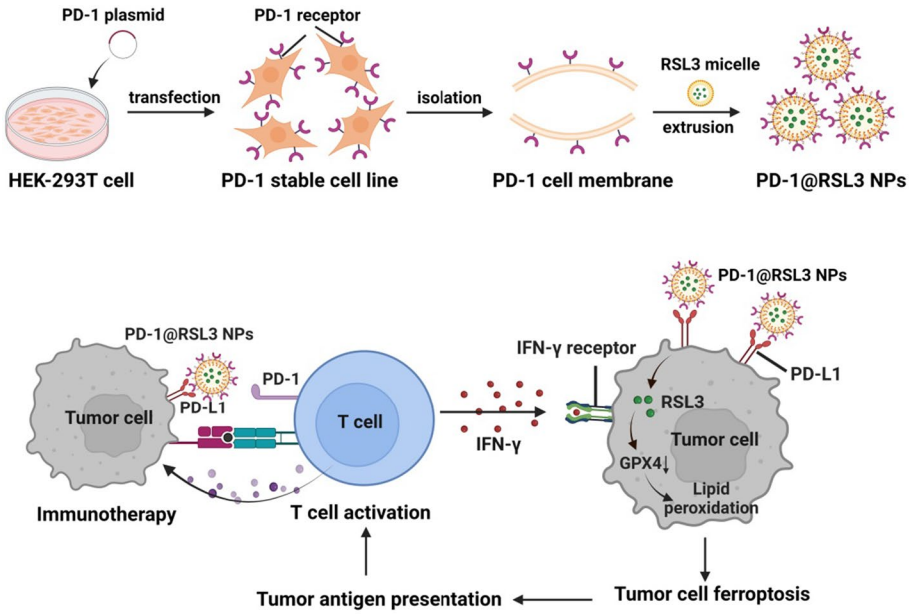


**Scheme 1** Schematic illustration of PD-1@RSL3 NPs preparation (**a**) and potentiated immunotherapy in TNBC (**b**)

micelles were coated with the PD-1 cell membrane to obtain PD-1@RSL3 NPs. We hypothesized that the PD-1 receptor on the surface of PD-1@RSL3 NPs could selectively bind with PD-L1 ligand overexpressed in TNBC cells and then disrupt the PD-1/PD-L1 inhibitory axis, triggering the antitumor immune response. Meanwhile, the released RLS3 from PD-1@RSL3 NPs and increased IFN-γ secretion through PD-L1 blockade synergistically promote tumor cell ferroptosis, amplifying the antitumor immune response.

## Experimental section

### Materials

RSL3 was purchased from Meilun (Dalian, China). Ferrostatin 1 and DSPE-PEG2000 were obtained from MCE (Shanghai, China). The lipid peroxidation probe C11 BODIPY 581/591 and Lipofectamine 3000 were purchased from Invitrogen (USA). The 4′,6-diamidino-2-phenylindole (DAPI), lipid peroxidation MDA kit, dioctadecyloxacarbocyanine perchlorate (DiO), 1′-dioctadecyl-3,3,3′,3′-tetramethylindocarbocyanine perchlorate (DiL) and Cell Counting Kit-8 were purchased from Beyotime (Shanghai, China). All the antibodies used for blocking and flow analysis in this study were purchased from Biolegend (USA). PD-1 and $Na^+K^+$ ATPase antibodies were purchased from Abcam (Shanghai, China). Anti-GPX4 antibody and HRP Anti-Goat IgG (H + L) were purchased from Abclonal (Wuhan, China). Serum tumor necrosis factor-alpha (TNF-α) and interferon-γ (IFN-γ) ELISA kits were purchased from Keygen Biotech (Jiangsu, China). DSPE-PEG2000-CY5.5 was purchased from Xian Ruixi (Shanxi, China). The mouse PD-1 plasmid was obtained from ORIENE (MR227347L4V). Dulbecco's modified Eagle's medium (DMEM) and fetal bovine serum (FBS) were purchased from Gibco (Shanghai, China).

### Preparation of the PD-1 stable cell line

Human embryonic kidney cells HEK293T were cultured in a medium containing 10% fetal bovine serum (FBS) and incubated at 37 °C 5% $CO_2$. A lentiviral vector containing the mouse PD-1 gene with a green fluorescent protein (GFP) tag was transfected into HEK293T cells with Lipofectamine 3000 reagent. The transfected cells were cultured and selected under puromycin screening (5 μg/mL). Stable cell lines with PD-1-GFP expression were obtained from single-cell colonies using the limited dilution method.

### Synthesis of PD-1 membrane-coated RSL3 nanoparticles

RSL3-loaded micelles were prepared using DSPE-PEG2000. 5 mg of DSPE-PEG2000 and 5 mg of RSL3 were dissolved in a Solanum-type flask containing an appropriate amount of acetonitrile. Acetonitrile was removed by evaporation on a rotary steamer. 20 mL of deionized water was added to hydrate for 30 min at 37 ℃ on a rotary steamer, and the solution was poured into a small beaker and placed in a magnetic agitator to stir for 30 min at room temperature. The unencapsulated RSL3 was removed with a 0.45 μm filter. Finally, the micellar solution was freeze-dried and stored in argon at −20 °C for further use. The loading of RSL3 in micelles was analyzed by a high-performance liquid chromatography (HPLC) system (Waters e2695) and a Phenomenex Gemini C18 column. The mobile phase consisted of a mixture of acetic acid aqueous solution (1%, v/v) and acetonitrile (40:60, v/v) at a constant flow rate of 1.0 mL/min. Fifty microliters of the solution were injected into the HPLC and then detected at a wavelength of 214 nm.

Cell membranes with stable PD-1-GFP expression were prepared using ultracentrifugation from a stable cell line. Briefly, cells were collected and crushed on the ice at least 50 times with a Dounce homogenizer, and the supernatant was centrifuged at 32,000 rpm for 4 h. The plasma membrane fragment was washed with HM buffer (0.25 M sucrose, 1 mM EDTA, 20 mM Hepes–NaOH, pH 7.4, and protease inhibitor cocktail) and resuspended in phosphate-buffered saline (PBS). PD-1 cell membrane-coated RSL3 NPs were prepared by the coextrusion method. RSL3-loaded micelles and PD-1 cell membrane were mixed and extruded through a 1 μm polycarbonate membrane at least 20 times and then through a 0.4 μm polycarbonate membrane at least 20 times to obtain PD-1@RSL3 NPs.

### Characterization of PD-1@RSL3 NPs

The size distribution and surface charge of the nanoparticles were measured at room temperature using a size and ζ potential meter (Microtrac, Nanotrac Wave II). For morphology analysis, nanoparticles were dropped on glow-discharged carbon-coated copper grids and then negatively stained with 2% uranyl acetate. The morphology of the nanoparticles was detected with a JEM 1011 microscope (JEOL, Japan). The stability of the nanoparticles was determined by measuring the size change in 10% sucrose solution at 4 °C. The size was examined every 2 days for 2 weeks.

### PD-1 expression analysis

Western blotting was used to evaluate PD-1 expression in the stable cell line and PD-1@RSL3 NPs. Briefly, total protein was quantified with a BCA assay kit

(Beyotime). The protein solutions containing equal amounts of protein were separated by SDS–PAGE and transferred to a polyvinylidene fluoride (PVDF) membrane. The membrane was incubated with PD-1 antibody (Abcam) overnight at 4 °C. After washing three times, horseradish peroxidase-conjugated IgG (Abclonal) was added at room temperature for 2 h. The membrane was treated with an enhanced chemiluminescence (ECL) kit and imaged by a chemiluminescence system (Amersham Imager 680).

#### In vitro drug release

The drug release profile was determined by measuring the released RSL3 in PBS using the dialysis method. RSL3-loaded nanoparticles were transferred into a dialysis bag (MWCO = 3500) and incubated in 20 ml of PBS buffer (pH 7.4 and pH 5.0) at 37 ℃. The release of RSL3 from PD-1 NVs (1 mg/mL) was analyzed by high-performance liquid chromatography (HPLC) at an absorbance of 214 nm in PBS.

#### In vitro PD-L1 blockade analysis

PD-L1 blockade analysis was examined by detecting the reduced binding of PD-1@RSL3 NPs with breast cancer cells induced by anti-PD-L1 (aPD-L1). A cell membrane fluorescent probe DiO was used to label the cell membrane-coated RSL3 micelles. Primary breast cancer cells from mice bearing 4T1 tumor models were cultured in 12-well plates at a density of $2 \times 10^5$ cells. Before adding DiO-labeled RSL3 nanoparticles, aPD-L1 (20 μg/mL) was incubated with cancer cells for 4 h. PD-1@RSL3 NPs were added to the medium and incubated for 4 h. After removing the nonspecific binding nanoparticles, cancer cells were collected and analyzed by a CytoFLEX flow cytometer (Beckman, Cytoflex S) (gated on FITC).

#### In vivo biodistribution

1 million 4T1 cells were implanted into female Balb/c mice to establish a breast cancer mouse model. When the tumor size reached 50 $mm^3$, the mice were randomly divided into two groups. Both Blank@RSL3 NPs and PD-1@RSL3 NPs were labeled with Cy5.5 for visualization. The Cy5.5-labeled nanoparticles were then administered intravenously to the mice via the tail vein. After a 12-h period post-injection, the treated mice were imaged with the IVIS Spectrum system (Tanon ABL X5, China) and quantity.

#### Cellular uptake assay

The cellular uptake of PD-1@RSL3 NPs was detected in 4T1 cells by confocal laser scanning microscopy (CLSM). Breast cancer cells 4T1 were seeded into the well plate at $1 \times 10^4$ cells per well for 12 h. The next day, DiO-labeled PD-1@RSL3 NPs were added into the well for 4 h incubation at 37 ℃. After washing three times with PBS, cancer cells were stained with DAPI for 15 min. The internalized nanoparticles by 4T1 were analyzed by confocal laser scanning microscopy (CLSM) (Zeiss, LSM710).

#### Cytotoxicity assay

The cytotoxicity of PD-1@RSL3 NPs was examined in mouse 4T1 cells by CCK8 assay. 4T1 cells were seeded into 96-well plates at a density of $4 \times 10^3$ per well and cultured at

37 °C for 24 h. On the second day, the medium was replaced with fresh medium containing free RSL3, Blank@RSL3 NPs, or PD-1@RSL3 NPs with different RSL3 concentrations (0, 0.5, 1, 2.5, 3.5, 5, 7.5 μM). After 48 h of incubation, CCK-8 solution was added to each well and incubated for 2 h. The solution absorbance was measured on a microplate reader (TECAN, M200) at 450 nm. Experiments were repeated three times. In another experiment, 4T1 cells were treated with RSL3 (final concentration: 5 μM) and Fer-1 (final concentration: 0.5 μM) to assess the inhibitory effect of tumor ferroptosis induced by RSL3. The cell viability of treated cells were evaluated by CCK8 assay.

#### GPX4 downregulation analysis

GPX4 downregulation was examined in 4T1 cells treated by western blot analysis. Briefly, 4T1 cells were seeded in a six-well plate overnight at 37 °C. The cells were treated with PBS, RSL3, Blank@RSL3 NPs, or PD-1@RSL3 NPs (RSL3: 5 μM) for 48 h. Cell lysates containing the same protein (20 μg) were subjected to SDS–PAGE separation and transferred to PVDF membranes. The membrane was incubated with GPX4 or β-actin antibodies at 4 °C overnight. After washing three times, the membrane was incubated with horseradish peroxidase-conjugated IgG. The membrane was incubated with an enhanced chemiluminescence (ECL) kit and imaged by a chemiluminescence system (Amersham Imager 680).

#### Lipid peroxidation assay

Malondialdehyde (MDA) accumulation in cancer cells was detected using the Lipid Peroxidation MDA Assay Kit (Beyotime). Breast cancer cells were treated with PBS, RSL3, Blank@RSL3 NPs, PD-1@RSL3 NPs, or Fer-1 + PD-1@RSL3 NPs (containing 5 μM RSL3) for 48 h. The cells were lysed on ice with RIPA buffer containing 1 mM PMSF for 30 min and centrifuged at 4 °C at 12,000 × g for 10 min. The supernatant absorbance was determined at 532 nm using a microplate reader (TECAN, M200).

#### ROS production assay

The ROS production assay was analyzed using the fluorescence probe C11 BODIPY®581/591 by flow cytometry and fluorescence microscopy. For flow cytometry analysis, 4T1 cells were seeded into a six-well plate for 12 h. On the second day, the cells were treated with PBS, RSL3, Blank@RSL3 NPs, PD-1@RSL3 NPs, or Fer-1 + PD-1@RSL3 NPs (RSL3: 5 μM) for 6 h. The cells were incubated with C11BODIPY®581/591 (final concentration: 10 μM) for 30 min at 37 ℃. After washing with PBS, the cells were digested and collected for flow cytometry analysis with 488 nm excitation and 510 nm emission filters.

Lipid peroxidation was also evaluated by fluorescence microscopy imaging using C11 BODIPY®581/591. Breast cancer cells were seeded into the well plate with $6 \times 10^4$ cells for 12 h. The cells were treated with PBS, RSL3, Blank@RSL3 NPs, PD-1@RSL3 NPs, or Fer-1 + PD-1@RSL3 NPs (RSL3: 5 μM) for 6 h and then incubated with C11BODIPY®581/591 for 30 min. The cells were imaged by the CLSM system with 488 nm and 510 nm excitation filters.

### In vivo antitumor efficacy

All animal experiments were conducted in accordance with the National Institutes of Health Guidelines for the Care and Use of Laboratory Animals, and the guidelines were approved by the Animal Protection and Utilization Committee of Taizhou University (Taizhou, Zhejiang). Female BALB/c mice (6 weeks) were purchased from Zhejiang Weitong Lihua Experimental Animal Technology Co., Ltd. The tumor model was prepared by subcutaneous injection of 4T1 cells ($1 \times 10^6$ cells/mouse) into the right flank of BALB/c mice. The mice were randomly divided into six groups on the seventh day after tumor inoculation. The mice received five doses of *i.v.* injection of PBS, RSL3 (5 mg/kg), Blank@RSL3 NPs (NVs: 25 mg/kg, protein mass; RSL3: 5 mg/kg), PD-1 NVs (NVs: 25 mg/kg, protein mass), aPD-L1 + RSL3 NPs (aPD-L1: 2.0 mg/kg; RSL3: 5 mg/kg), or PD-1@RSL3 NPs (NVs: 25 mg/kg, protein mass RSL3: 5 mg/kg) every 3 days. The tumor volume and body weight were monitored at the indicated timepoints. Tumor volume ($V$) was calculated as $V = d^2 \times D/2$, where d is the shortest, and D is the longest diameter of the tumor.

### Flow cytometry

Tumor tissues were minced into small pieces of approximately 1 mm3 and digested in DMEM containing DNase I (0.25 mg/mL, Sigma-Aldrich) and collagenase IA (0.5 mg/mL Sigma-Aldrich) at 37 °C for 4 h. The cell suspension was filtered with a 200-mesh strainer and collected at 1000 rpm for 5 min. The collected cells were treated with the Zombie Violet dye Fixable Viability Kit and blocked with the FC blocking antibody CD16/32 (clone 93). Specific fluorescent antibodies against CD45 (PerCP-Cyanine5.5; clone 30-F11), CD3 (APC; clone 17A2), CD8a (PE; clone 53–6.7), CD4 (FITC; clone GK1.5), CD11b (FITC; clone M1/70), CD80 (PECyanine7; clone 16-10A1) CD86 (APC; clone GL-1), and Foxp3 (Alexa Fluor® 647; Clone MF-14) (Biolegend) were used. After three washes, the cell suspensions were analyzed on a CytoFLEX flow cytometer (Beckman) with CytoExpert software (Beckman Coulter). Tumor-infiltrated $CD8^+$ T cells ($CD45^+CD3^+CD8^+$), dendritic cells (DCs) ($CD45^+CD11c^+CD80^+CD86^+$), and regulatory T cells (Tregs) ($CD45^+CD3^+CD4^+Foxp3^+$) were analyzed.

### Cytokine detection

Serum samples were isolated from mice treated with PBS, RSL3, Blank@RSL3 NPs, PD-1 NVs, aPD-L1 + RSL3 NPs, or PD-1@RSL3 NPs. Interferon-γ (IFN-γ) and tumor necrosis factor (TNF-α) were analyzed with ELISA kits (Kaiji, China) according to the manufacturer's protocols.

### Tissue section staining

The major organs (including liver, spleen, kidney, heart, and lung) and tumor tissues were excised from mice treated with different formulations. For H&E staining, the tissues were treated with paraffin and stained with hematoxylin and eosin. The tumor section was also analyzed by immunostaining using Ki67 and calreticulin (CRT) antibodies.

### Biosafety assay

The blood samples from mice receiving PBS, RSL3, Blank@RSL3 NPs, PD-1 NVs, aPD-L1 + RSL3 NPs, or PD-1@RSL3 NPs were analyzed by an automatic biochemistry analyzer (Olympus AU2700). The levels of alanine aminotransferase (ALT), aspartate aminotransferase (AST), uric acid (UA), and creatinine (Cr) in the supernatants were determined.

### Statistical analysis

All the data are expressed as the mean ± standard deviation. Statistical analysis was performed using SPSS software. One-way or two-way analysis of variance (ANOVA) and Tukey post hoc tests were used to calculate the statistical significance. The log-rank test was used to determine the survival of mice. The threshold of statistical significance was $P < 0.05$, $^{*}P < 0.05$, $^{**}P < 0.01$, $^{***}P < 0.001$.

## Results and discussion

### Preparation and characterization of PD-1@RSL3 NPs

We established a stable cell line expressing the mouse PD-1 receptor by transfecting a lentiviral plasmid containing the PD-1 gene and green fluorescent protein (GFP) tag into HEK-293 T cells (Additional file 1: Fig. S1). HEK-293 T cells are widely used for stable cell construction due to their high transfection efficiency, good protein expression capability (especially membrane receptors), and easy maintenance. The stable cell lines simultaneously expressed PD-1-GFP fusion protein on the cell membrane (Fig. 1a, and Additional file 1: Fig. S2). The plasma membrane of the stable

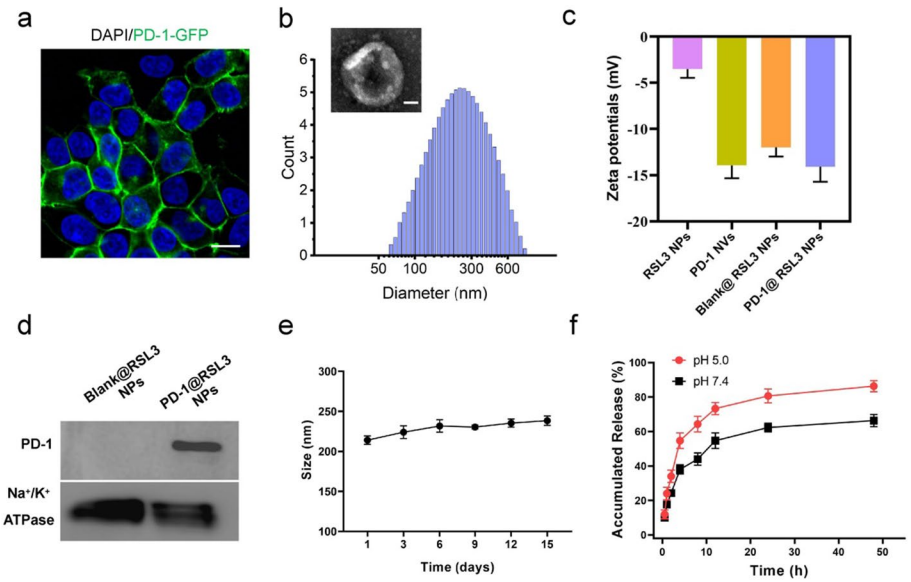


**Fig. 1** Characterization of the PD-1 membrane-coated ferroptosis nanoinducer. **a** CLSM imaging analysis of PD-1-GFP expression in the HEK-293 T-PD-1 stable cell line. Scale bar: 20 μm. **b** Size distribution and morphology analysis of PD-1@RSL3 NPs. Scale bar: 50 nm. **c** Surface charge of RSL3 NPs, PD-1 NVs, Blank@RSL3 NPs, and PD-1@RSL3 NPs. **d** Western blot analysis confirmed the PD-1 expression in PD-1@RSL3 NPs. **e** In vitro stability analysis of PD-1@RSL3 NPs by measuring the size changes at 4 ℃. f. Drug release profile of PD-1@RSL3 NPs in vitro

cell lines was isolated to transform into nanovesicles. The PD-1 receptor-presenting nanovesicles (PD-1 NVs) were hollow sphere nanostructures with good cytocompatibility in HEK-293 T cells (Additional file 1: Figs. S3 and S4, ESI). Given the ferroptosis induced by inhibiting glutathione peroxidase 4 (GPX4) activities, ferroptosis inducer RSL3-loaded micelles were prepared using DSPE-PEG2000 (Additional file 1: Figs. S5 and S6, ESI) and then coated with PD-1 cellular membrane, named PD-1@RSL3 NPs. Dynamic light scattering (DLS) and transmission electron microscopy (TEM) analysis revealed that PD-1@RSL3 NPs have a mean diameter of 202.4 nm (polymer dispersity index: 0.25) and spherical nanostructure (Fig. 1b and Additional file 1: Fig. S7). The surface charge of PD-1@RSL3 NPs was determined to be -12.4 mV (Fig. 1c). Western blot confirmed the reserved PD-1 proteins in PD-1@RSL3 NPs (Fig. 1d). PD-1@RSL3 NPs displayed good colloidal stability in PBS solution (Fig. 1e). In vitro drug release profile demonstrated that RSL3 could be sustainably released from PD-1@RSL3 NPs in 48 h, with slightly faster release at pH 5.0 than that at neutral pH (Fig. 1f).

#### In vitro biological activities of PD-1@RSL3 NPs

Cancer cells prevent immune attack by inducing T-cell exhaustion through the PD-L1/PD-1 axis (Fang et al. 2023). Owing to the PD-L1/PD-1 interaction, we evaluated the PD-L1 blockade property of PD-1@RSL3 NPs. A murine TNBC cell line 4T1, which overexpressed PD-L1 ligands on the surface (Wang et al. 2021), was used to investigate the binding properties of PD-1@RSL3 NPs. PD-1@RSL3 NPs were stained with DiO fluorescent dye. Before being incubated with DiO-labeled nanoparticles, breast cancer cells were pretreated with PD-L1 antibodies (aPD-L1) for 4 h. Flow cytometry analysis indicated a twofold tumor binding in 4T1 cells treated with PD-1@RSL3 NPs compared with that in the Blank@RSL3 NPs group, suggesting a preferred binding property of PD-1@RSL3 NPs with 4T1 cells. Moreover, pretreatment with aPD-L1 significantly decreased the binding of PD-1@RSL3 NPs with cancer cells (Fig. 2a, b). These results verified that the binding of PD-1@RSL3 NPs with 4T1 cells was realized through the PD-L1/PD-1 interaction. The biodistribution of PD-1 membrane-coated nanoparticles was assessed in mice bearing 4T1 tumors. The findings revealed that PD-1 decoration notably enhanced the targeted accumulation of nanoparticles specifically in tumor tissues (Fig. 2c, d). We next evaluated the cellular uptake and cytotoxicity of PD-1@RSL3 NPs. DiO-labeled PD-1@RSL3 NPs were incubated with 4T1 cells for 4 h. The fluorescent dots distributed in the perinuclear area demonstrated that PD-1@RSL3 NPs could be efficiently uptaken by breast cancer cells (Additional file 1: Fig. S8). Cytotoxicity was evaluated by measuring the cell viability of 4T1 cells treated with different formulations via CCK-8 assay. A dose-dependent killing effect was observed in free RSL3 and RSL3-loaded nanoparticles after 48 h of treatment (Fig. 2e and Additional file 1: Fig. S9). To reveal the potential ferroptosis, we used ferrostatin-1 (Fer-1) to inhibit tumor cell death caused by RSL3 (Additional file 1: Fig. S10) (Miotto et al. 2020). Notably, the addition of Fer-1 significantly decreased the killing effect of PD-1@RSL3 NPs, validating tumor cell ferroptosis induced by PD-1@RSL3 NPs (Fig. 2f).

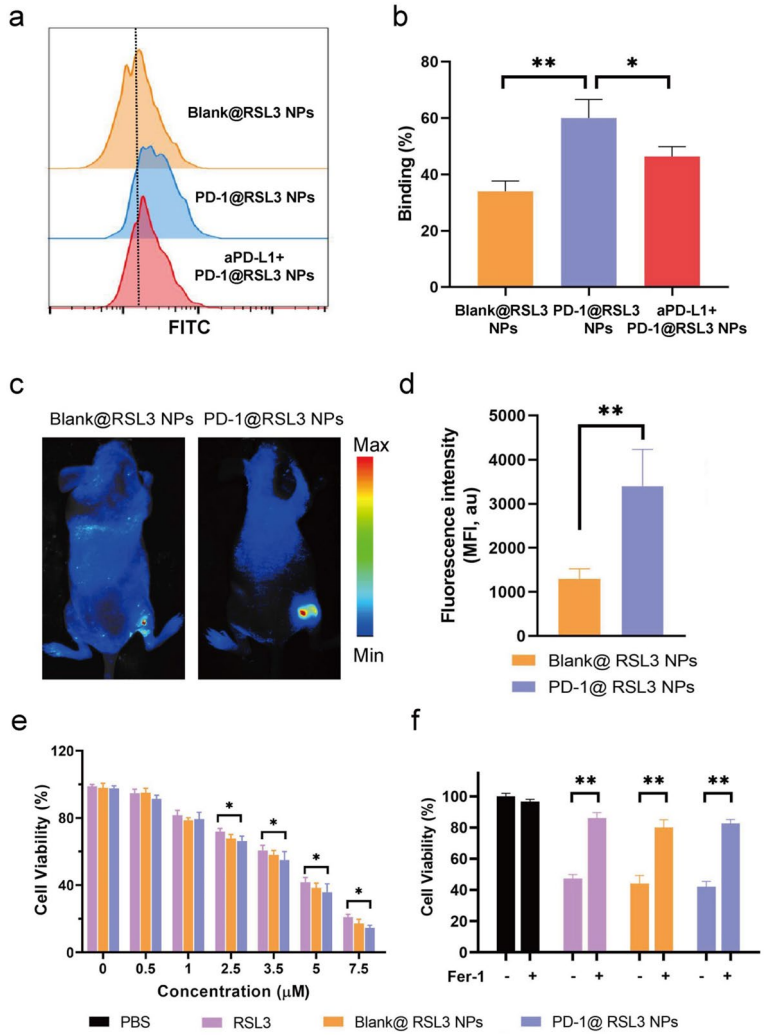


**Fig. 2** In vitro PD-L1 blockade and cytotoxicity analysis of PD-1@RSL3 NPs. **a** Flow cytometric analysis showed that PD-1 NVs binding with 4T1 cells significantly decreased after adding aPD-L1. **b** Quantitation of 4T1 cells bound to PD-1 NVs with or without aPD-L1 pretreatment. **c**, **d** In vivo biodistribution (**c**) and quantitative analysis (**d**) of Cy5.5-labeled Blank@RSL3 NPs and PD-1@RSL3 NPs in mice bearing 4T1 xenografts was evaluated by IVIS system. **e** Cytotoxicity analysis of PD-1@RSL3 NPs containing different RSL3 concentrations (ranging from 0 to 7.5 μM) against breast cancer cells in vitro. **f** Ferroptosis inhibitor Fer-1 reversed the tumor-killing induced by PD-1@RSL3 NPs in 4T1 cells (RSL3: 5 μM; Fer-1: 0.5 μM)

### PD-1@RSL3 NPs boosted tumor cell ferroptosis in TNBC cells

Furthermore, we explored the ferroptosis mechanism induced by PD-1@RSL3 NPs. Western blot results revealed that GPX4 expression was significantly inhibited in 4T1 cells treated with RSL3 or RSL3 NPs, suggesting impaired antioxidative activities (Fig. 3a). Considering the critical role of GPX4 in maintaining redox homeostasis (Yang et al. 2014), we hypothesized that the impaired antioxidative function might contribute to lipid peroxidation in cancer cells. Lipid peroxidation was examined by monitoring the reactive oxygen species (ROS) production and malondialdehyde (MDA) accumulation in breast cancer cells. A lipid peroxide fluorescence probe C11 BODIPY®581/591 could react with hydroxyl radicals and display different fluorescence (reduced prototype emitted at 591 nm; oxidized type emitted at

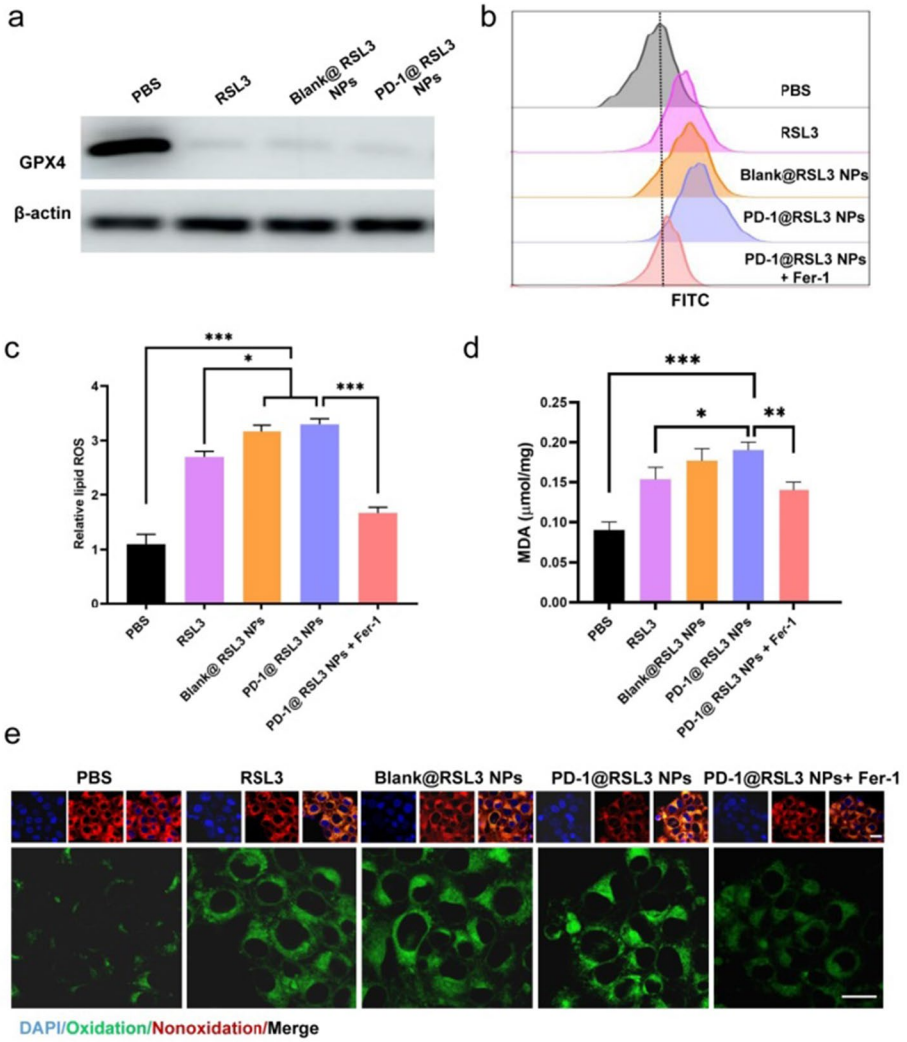


**Fig. 3** PD-1@RSL3 NPs boosted tumor cell ferroptosis in breast cancer cells. **a** Western blot analysis confirmed the downregulated GPX4 expression in 4T1 cells treated with PD-1@RSL3 NPs for 48 h. **b, c** Flow cytometry analysis and the normalized ratio of lipid ROS production in 4T1 cells using a fluorescence probe C11 BODIPY®581/591. **d** Lipid peroxidation analysis in 4T1 cells treated with different formulations via MDA assay. **e** CLSM analysis of lipid peroxidation (green) using C11 BODIPY®581/591 in 4T1 cells. Scale bar: 20 μm. The concentrations of RSL3 and IFN-γ used in **a**–**e** were 5 μM and 100 ng/ml, respectively

510 nm) (Zhao et al. 2023), was used to determine lipid ROS accumulation in 4T1 cells. Flow cytometry results demonstrated that RSL3 contributed to moderate ROS production, while PD-1@RSL3 NPs induced much higher ROS production in 4T1 cells than PBS (Fig. 3b, c). MDA, one of the most common biomarkers in polyunsaturated fatty acid (PUFA) peroxidation, was used to determine the extent of lipid peroxidation in this study (Tsikas 2017). PD-1@RSL3 NPs treatment induced a 2.1-fold increase in MDA production compared with the control group, suggesting elevated PUFA peroxidation (Fig. 3d). CLSM imaging verified that PD-1@RSL3 NPs generated enhanced ROS accumulation (green fluorescence) (Fig. 3e). Fer-1 treatment significantly depleted ROS production and lipid peroxidation induced by PD-1@RSL3 NPs (Fig. 3c, d). These results indicated that PD-1@RSL3 NPs inhibited the antioxidative

defense system and promoted the lipid peroxidation in 4T1 cells, ultimately leading to enhanced tumor cell ferroptosis.

#### IFN-γ secretion and its effect on tumor cell ferroptosis

Several reports have indicated that PD-L1 blockade-activated $CD8^+$ T cells promote tumor cell ferroptosis by increasing IFN-γ secretion, improving the efficacy of immunotherapy (Song et al. 2021). Therefore, we explored whether PD-1@RSL3 NPs could promote IFN-γ secretion in mice bearing TNBC xenografts. After five treatments, mice were sacrificed to isolate the serum. PD-1 NVs triggered 2.2-fold IFN-γ secretion, compared with Blank NVs (Fig. 4a), showing the activated immune response in vivo. Moreover, the addition of IFN-γ exacerbated the tumor cell death induced by PD-1@RSL3 NPs (Fig. 4b). To confirm if the type of cell death is ferroptosis, we investigated the lipid peroxidation and ROS level in cells treated with IFN-γ and different formulations. The finding revealed that IFN-γ addition remarkably enhanced the MDA and ROS production

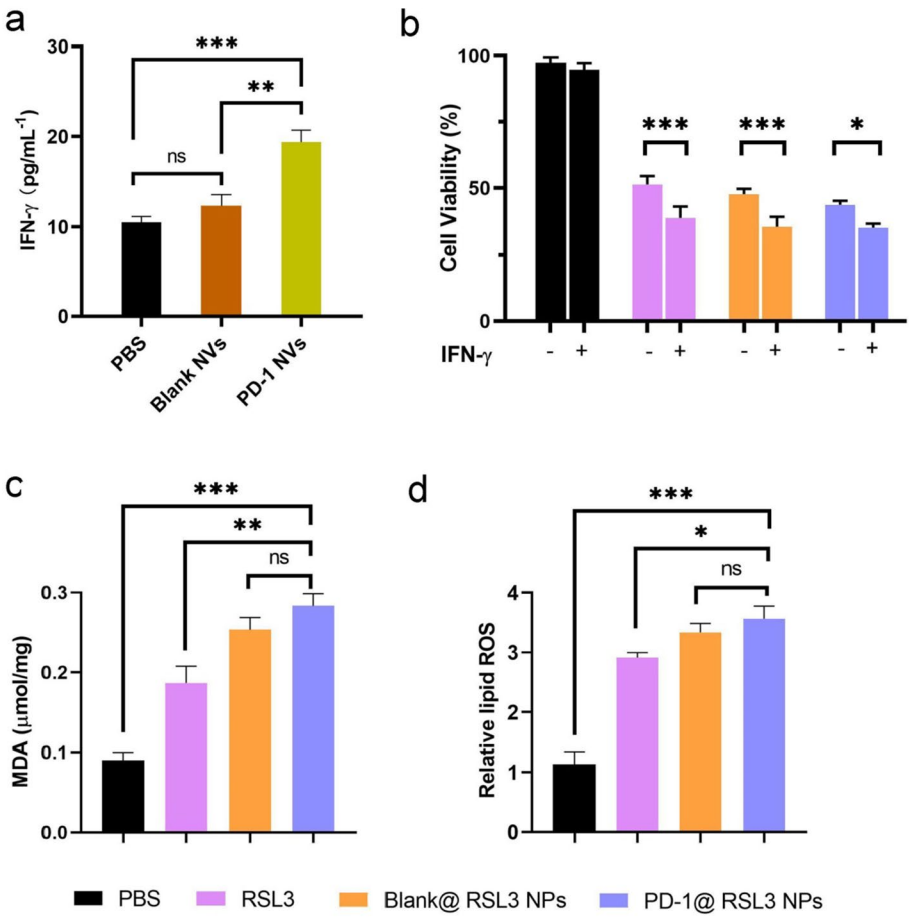


**Fig. 4** In vivo IFN-γ secretion induced by PD-1 NVs and pro-ferroptosis effect in breast cancer cells. **a** Serum IFN-γ level in mice bearing 4T1 xenografts five times after PD-1 NVs treatment. **b** IFN-γ exacerbated the ferroptosis of 4T1 cells induced by PD-1@RSL3 NPs (IFN-γ: 100 ng/ml; RSL3: 5 μM). **c** Lipid peroxidation analysis in 4T1 cells treated with IFN-γ and different formulations via MDA assay (IFN-γ: 100 ng/ml; RSL3: 5 μM). **d** ROS production analysis in 4T1 cells treated with IFN-γ and different formulations (IFN-γ: 100 ng/ml; RSL3: 5 μM)

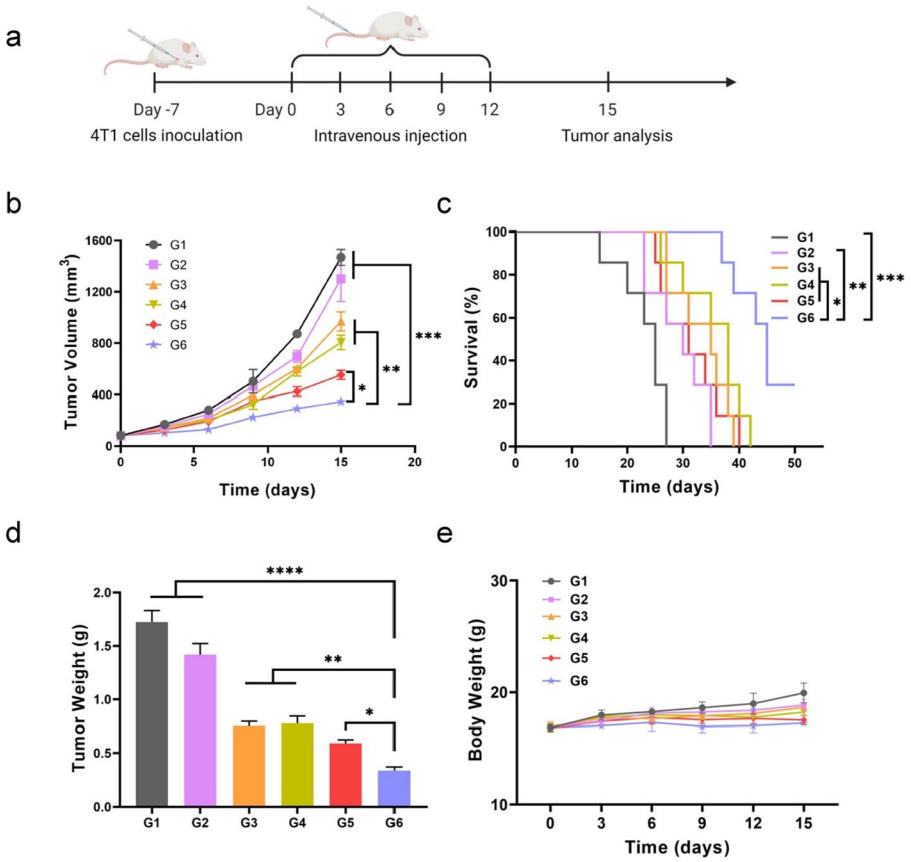


**Fig. 5** In vivo antitumor analysis of PD-1@RSL3 NPs. **a** Schedule of PD-1@RSL3 NPs treatment in 4T1 tumor-bearing mice. PBS, RSL3 (5 mg/kg), Blank@RSL3 NPs (NVs: 25 mg/kg, protein mass; RSL3: 5 mg/kg), PD-1 NVs (NVs: 25 mg/kg, protein mass), aPD-L1 + RSL3 NPs (aPD-L1: 2.0 mg/kg; RSL3: 5 mg/kg), or PD-1@RSL3 NPs (NVs: 25 mg/kg, protein mass RSL3: 5 mg/kg). **b** Tumor growth curves of 4T1-tumor-bearing mice receiving different treatments ($n \geq 5$). **c** Survival rates of mice receiving different treatments. **d** Excised tumor weight in different groups. **e** Body weight of mice receiving different treatments. G1, PBS; G2, RSL3; G3, Blank@RSL3; G4, PD-1 NVs; G5, aPD-L1 + RSL3 NPs; G6, PD-1@RSL3. Data were shown as mean ± SD. *P* values are from one-way ANOVA followed by Tukey's post-test (B, D) or log-rank (Mantel–Cox) test (C). $^{*}P < 0.05$, $^{**}P < 0.01$, $^{***}P < 0.001$

in cells treated with PD-1@RSL3 NPs (Fig. 4c, d). These results indicated that combined use of IFN-γ and PD-1@RSL3 NPs exacerbated tumor ferroptosis of breast cancer cells.

### In vivo antitumor analysis of PD-1@RSL3 NPs

Given the PD-L1 blockade property and increased IFN-γ secretion effect, we expected that PD-1@RSL3 NPs could exhibit enhanced antitumor efficacy in vivo. We established a breast cancer mouse model by injecting 4T1 cells into BALB/c mice (Fig. 5a). RSL3 NPs and Blank@RSP3 NPs slightly delayed tumor growth after five treatments, while two combined treatment groups demonstrated remarkable tumor growth suppression in vivo (Fig. 5b). PD-1@RSL3 NPs showed more tumor suppression than aPD-L1 + RSL3 NPs, confirming the unique advantage of PD-1 membrane-coated nanoparticles as the delivery platform for cancer therapy (Fig. 5b). PD-1@RSL3 NPs also extended the survival of mice bearing TNBC xenografts (Fig. 5c). The average weight of excised tumors in

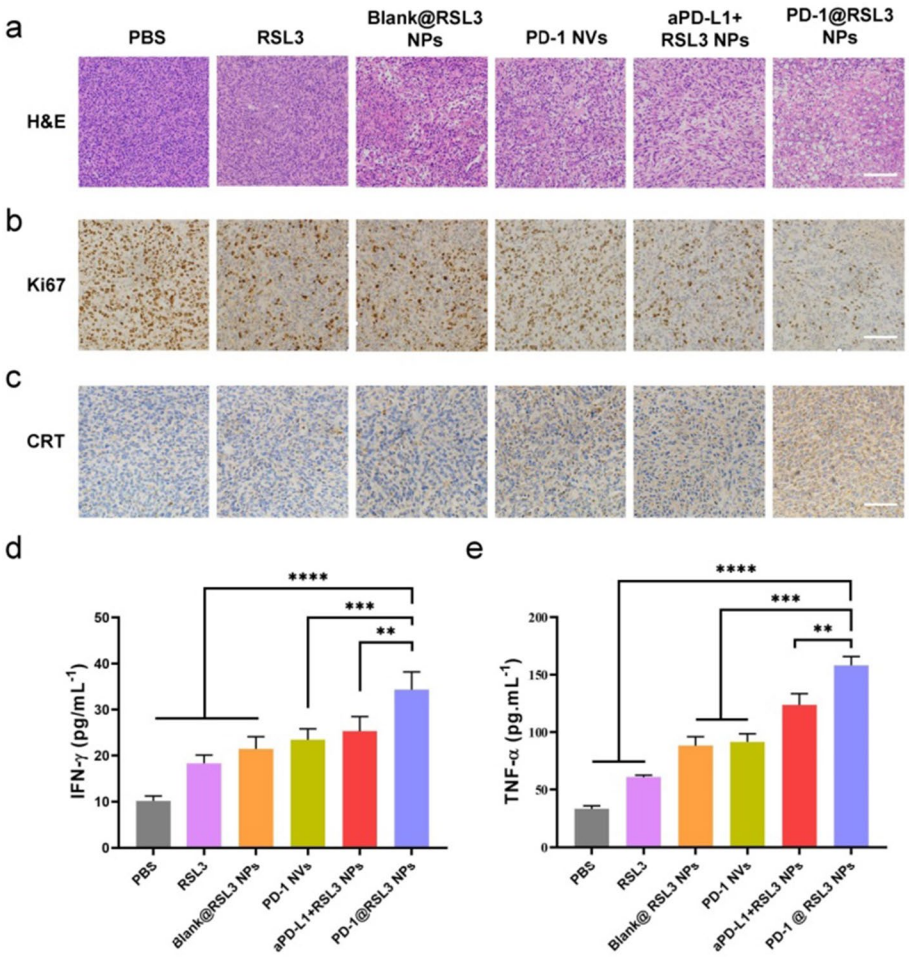


**Fig. 6** Tumor tissue staining showed that PD-1@RSL3 NPs inhibited tumor growth and enhanced tumor immunogenicity in mice bearing breast cancer xenograft. **a** H&E staining of tumor tissues. Scale bar: 100 μm. **b** Ki67 staining indicated delayed tumor growth in mice treated with PD-1@RSL3 NPs. Scale bar: 100 μm. **c** Calreticulin (CRT) exposure analysis suggested that PD-1@RSL3 NPs significantly enhanced the ICD-associated immunogenicity. **d** Serum IFN-γ analysis in mice. **e** TNF-α analysis in different groups. *P* values are from one-way ANOVA followed by Tukey's post-test (**d**, **e**)

the PD-1@RSL3 NPs group was lower than that in the aPD-L1 + RSL3 NPs (Fig. 5d and Additional file 1: Fig. S11). These results demonstrated the synergized antitumor efficacy of PD-1@RSL3 NPs in treating TNBC. The body weight changes indicated no noticeable weight loss during the treatment (Fig. 5e).

Furthermore, the therapeutic efficacy of PD-1@RSL3 NPs was examined by pathology analysis. Hematoxylin and eosin (H&E) staining showed apparent cell death in the PD-1@RSL3 NPs group (Fig. 6a). In addition to H&E staining analysis, we performed Ki67 immunostaining for the cell proliferation assay. The reduced Ki67 staining in PD-1@RSL3 NPs demonstrated markedly decreased cell proliferation ability (Fig. 6b). Calreticulin (CRT) exposure analysis indicated that PD-1@RSL3 NPs induced ICD in mice bearing 4T1 models, suggesting enhanced immunogenicity of TNBC (Fig. 6c). The serum pro-inflammatory factors IFN-γ and tumor necrosis factor-α (TNF-α) were also determined. PD-1@RSL3 NPs treatment promoted approximately a threefold IFN-γ

secretion and fivefold TNF-α production compared with the control group, showing a robust antitumor immune response induced by PD-1@RSL3 NPs (Fig. 6d, e).

#### PD-1@RSL3 NPs elicited antitumor immune response in vivo

To reveal the critical role of effector T cells in tumor killing, we investigated the infiltration of $CD8^+$ T cells in the tumor microenvironment after treatment with PD-1@RSL3 NPs (Additional file 1: Fig. S12). Flow cytometry analysis showed a 3.1-fold increase of tumor-infiltrating $CD8^+$ T cells in the PD-1@RSL3 NPs than that in the PBS group (Fig. 7a). Notably, PD-1@RSL3 NPs activated more $CD8^+$ T cells than aPD-L1 + RSL3 NPs (Fig. 7b). The increased presence of $CD8^+$ T cells in tumors validated the activated immune system induced by our nanoparticles. In addition, PD-1@RSL3 NPs promoted 1.5-fold increase in DC maturation than aPD-L1 + RSL3 NPs (Fig. 7c, d and Additional file 1: Fig. S13), indicating an enhanced capability of tumor–antigen recognition and presentation. Consistently,, the number of regulatory T (Treg) cells in the tumor microenvironment decreased significantly in response to PD-1@RSL3 NPs (Fig. 7e, f

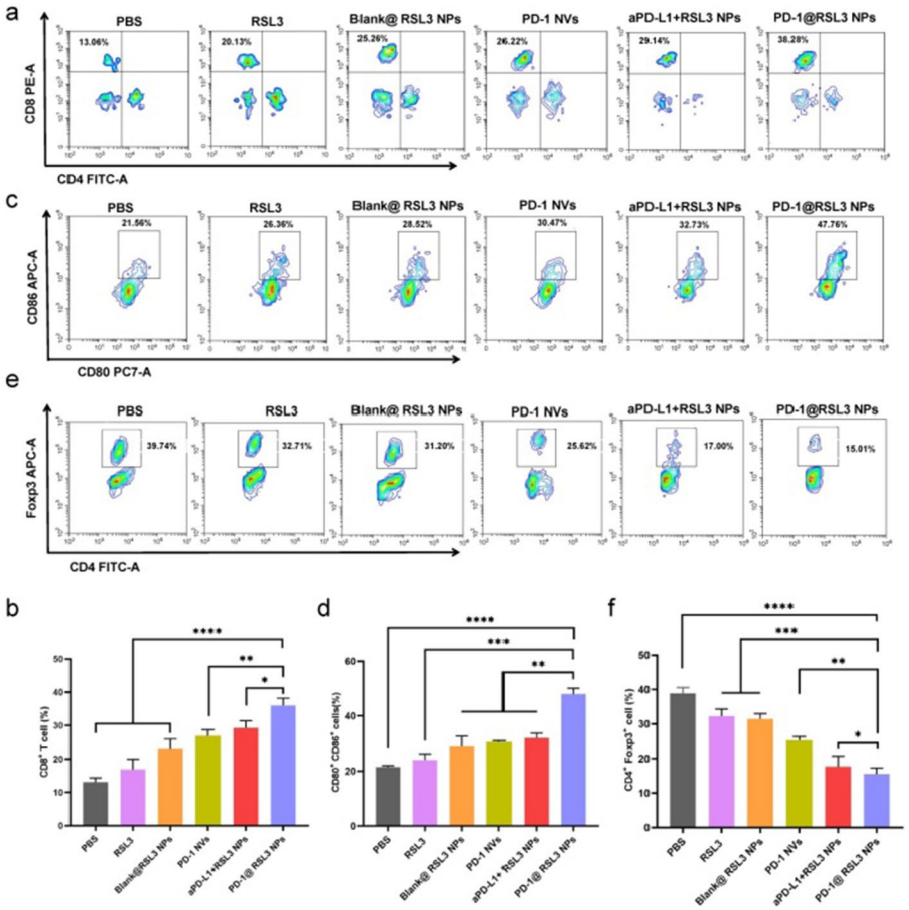


**Fig. 7** PD-1@RSL3 NPs induced a solid antitumor immune response in mice bearing breast cancer xenografts. **a, b** Flow cytometry analysis and percentage of $CD8^+$ T-cell infiltration (gated on $CD8^+$ T cells). **c**, **d** Flow cytometry analysis and percentage of dendritic cells (gated on $CD80^+CD86^+$ cells). **e**, **f** Flow cytometry analysis and percentage of Treg cells (gated on $CD4^+Foxp3.^+$ cells). *P* values are from one-way ANOVA followed by Tukey's post-test (**b**, **d**, **f**)

and Additional file 1: Fig. S14), suggesting a reduction in the inhibitory effect of Treg cells on $CD8^+$ T cells. Taken together, these findings demonstrate that the combination of immune checkpoint blockade and tumor ferroptosis induced by PD-1@RSL3 NPs boosted a strong antitumor immune response.

Biosafety concerns remain a major challenge of biomaterials for further application. In vivo potential toxicity was examined by histological examination of major organs and serum biochemistry assays. H&E staining images demonstrated that injection of PD-1@RSL3 NPs did not produce noticeable side effects on mice bearing breast cancer models (Additional file 1: Fig. S15). Serum biochemistry assay showed that hepatic and renal function indicators were comparable to the values of the control group (Additional file 1: Fig. S16), showing no detectable toxicity to normal organs.

## Conclusions

We developed PD-1 membrane-coated RSL3 nanoparticles to promote tumor cell ferroptosis and activate antitumor immunity toward breast cancer. The PD-1@RSL3 NPs could block the PD-L1 ligand and promote tumor cell ferroptosis caused by GPX4 inhibition in TNBC. The tumor cell ferroptosis enhanced the immunogenicity of TNBC and augmented the PD-L1 blockade-mediated antitumor immune response. Combining ferroptosis inducer and PD-L1 nanoblockade significantly delayed tumor progression and extended the survival of mice bearing breast cancer xenograft. This study demonstrates an elegant example of using PD-1 membrane-coated ferroptosis nanoinducer for enhanced cancer immunotherapy.

**Abbreviations**

| | |
|---|---|
| ICB | Immune checkpoint blockade |
| CTLA-4 | Cytotoxic T lymphocyte-associated protein 4 |
| PD-1 | Programmed cell death protein 1 |
| PD-L1 | Programmed death ligand 1 |
| ROS | Reactive oxygen species |
| TNBC | Triple-negative breast cancer |
| GPX4 | Glutathione peroxidase 4 |
| DAMPs | Damage-associated molecular patterns |
| ICD | Immunogenic cell death |

## Supplementary Information

The online version contains supplementary material available at https://doi.org/10.1186/s12645-023-00234-2.

**Additional file 1: Figure S1.** Plasmid map of lentiviral mouse PD-1 gene expression vector. **Figure S2.** Western blot analysis confirmed the PD-1 expression in the stable cell line. **Figure S3.** Morphology analysis of PD-1 NVs by TEM assay. **Figure S4.** In vitro biocompatibility analysis of PD-1 NVs in HEK-293 T cells via CCK8 assay. **Figure S5.** Size distribution of RSL3-loaded micelles detected by DLS. **Figure S6.** Morphology analysis of RSL3-loaded micelles detected by TEM. **Figure S7.** Morphology analysis of PD-1@RSL3 NPs detected by TEM assay. **Figure S8.** Cellular uptake of DiO-labeled PD-1@RSL3 NPs in 4T1 cells by fluorescence microscopy. **Figure S9.** Cytotoxicity analysis of free RSL3 against 4T1 cells via CCK8 assay. **Figure S10.** Fer-1 inhibited the tumor-killing caused by RSL3 in 4T1 cells via CCK8 assay. **Figure S11.** Representative images of excised tumors from mice receiving different treatments. **Figures S12–14.** Gating strategy used to identify $CD8^+$ T cells, DC and Treg among tumor-infiltrated immune cells. **Figure S15.** H&E staining of main organs from mice treated with PBS, RSL3, Blank@RSL3, PD-1 NVs, aPD-L1 + RSL3 NPs, and PD-1@RSL3. **Figure S16.** Liver function (ALT and AST) and kidney function (CR and UA) of the mice treated with PD-1@RSL3 NPs. **Figure S17.** Uncropped western blot images for Figs. 1d, 3a, and S2.

**Acknowledgements**

The authors gratefully acknowledge technical and financial support provided by Medical School of Taizhou University, China.

**Author contributions**
YM: methodology, investigation. YF: methodology, investigation. LH: investigation, software. NH: methodology, investigation. HX: investigation. XG: conceptualization, resources, supervision, writing—reviewing. ZZ: supervision, and funding. All authors reviewed and approved the final manuscript.

**Funding**
This study was supported by Zhejiang Provincial Natural Science Foundation of China (LY23C100001), Science and Technology Program of Taizhou City (22gya03), Taizhou Anti-Cancer Association special research project (TACA-C06).

**Availability of data and materials**
All data generated or analyzed during this study are included in this article.

## Declarations

**Ethics approval and consent to participate**
The protocols for the animal experiments were approved by Animal Protection and Utilization Committee of Taizhou University (Taizhou, Zhejiang). All animal experiments were conducted in accordance with the National Institutes of Health Guidelines for the Care and Use of Laboratory Animals.

**Consent for publication**
We give our consent for the manuscript to be published in Cancer Nanotechnology.

**Competing interests**
The authors declare no competing interests.

Received: 17 September 2023 Accepted: 30 October 2023
Published online: 13 November 2023

**References**

Carlino MS, Larkin J, Long GV (2021) Immune checkpoint inhibitors in melanoma. Lancet 398(10304):1002–1014
Chen X, Kang R, Kroemer G et al (2021) Broadening horizons: the role of ferroptosis in cancer. Nat Rev Clin Oncol 18(5):280–296
Dixon SJ, Lemberg KM, Lamprecht MR et al (2012) Ferroptosis: an iron-dependent form of nonapoptotic cell death. Cell 149(5):1060–1072
Fang W, Li L, Lin Z et al (2023) Engineered IL-15/IL-15Rα-expressing cellular vesicles promote T cell anti-tumor immunity. Extracell Vesicle 2:100021
Friedmann Angeli JP, Xavier da Silva TN, Schilling B (2022) CD8(+) T cells PUF(A)ing the flames of cancer ferroptotic cell death. Cancer Cell 40(4):346–348
Hassannia B, Vandenabeele P, Vanden Berghe T (2019) Targeting ferroptosis to iron out cancer. Cancer Cell 35(6):830–849
Jiang X, Stockwell BR, Conrad M (2021) Ferroptosis: mechanisms, biology and role in disease. Nat Rev Mol Cell Biol 22(4):266–282
Li J, Cao F, Yin HL et al (2020) Ferroptosis: past, present and future. Cell Death Dis 11(2):88
Li B, Fang T, Li Y et al (2022) Engineered T cell extracellular vesicles displaying PD-1 boost anti-tumor immunity. Nano Today 46:101606
Liang C, Zhang X, Yang M et al (2019) Recent progress in ferroptosis inducers for cancer therapy. Adv Mater 31(51):e1904197
Liao P, Wang W, Wang W et al (2022) CD8(+) T cells and fatty acids orchestrate tumor ferroptosis and immunity via ACSL4. Cancer Cell 40(4):365–378
Martin JD, Cabral H, Stylianopoulos T et al (2020) Improving cancer immunotherapy using nanomedicines: progress, opportunities and challenges. Nat Rev Clin Oncol 17(4):251–266
Meng QF, Zhao Y, Dong C et al (2021) Genetically programmable fusion cellular vesicles for cancer immunotherapy. Angew Chem Int Ed 60(50):26320–26326
Miotto G, Rossetto M, Di Paolo ML et al (2020) Insight into the mechanism of ferroptosis inhibition by ferrostatin-1. Redox Biol 28:101328
Rao L, Wu L, Liu Z et al (2020) Hybrid cellular membrane nanovesicles amplify macrophage immune responses against cancer recurrence and metastasis. Nat Commun 11(1):4909
Ren E, Liu C, Lv P et al (2021) Genetically engineered cellular membrane vesicles as tailorable shells for therapeutics. Adv Sci 8(21):e2100460
Robert C (2020) A decade of immune-checkpoint inhibitors in cancer therapy. Nat Commun 11(1):3801
Schoenfeld AJ, Hellmann MD (2020) Acquired resistance to immune checkpoint inhibitors. Cancer Cell 37(4):443–455
Shi L, Liu Y, Li M et al (2021) Emerging roles of ferroptosis in the tumor immune landscape: from danger signals to anti-tumor immunity. FEBS J 289(13):3655–3665
Singh S, Hassan D, Aldawsari HM et al (2020) Immune checkpoint inhibitors: a promising anticancer therapy. Drug Discov Today 25(1):223–229
Song R, Li T, Ye J et al (2021) Acidity-activatable dynamic nanoparticles boosting ferroptotic cell death for immunotherapy of cancer. Adv Mater 33(31):2101155
Tang D, Chen X, Kang R et al (2021) Ferroptosis: molecular mechanisms and health implications. Cell Res 31(2):107–125

Tsikas D (2017) Assessment of lipid peroxidation by measuring malondialdehyde (MDA) and relatives in biological samples: analytical and biological challenges. Anal Biochem 524:13–30
Ubellacker JM, Tasdogan A, Ramesh V et al (2020) Lymph protects metastasizing melanoma cells from ferroptosis. Nature 585(7823):113–118
Waldman AD, Fritz JM, Lenardo MJ (2020) A guide to cancer immunotherapy: from T cell basic science to clinical practice. Nat Rev Immunol 20(11):651–668
Wang W, Green M, Choi JE et al (2019) CD8(+) T cells regulate tumour ferroptosis during cancer immunotherapy. Nature 569(7755):270–274
Wang Y, Li X, Zheng D et al (2021) Selective degradation of PD-L1 in cancer cells by enzyme-instructed self-assembly. Adv Funct Mater 31(45):2102505
Wang L, Chen X, Yan C (2022a) Ferroptosis: an emerging therapeutic opportunity for cancer. Genes Dis 9(2):334–346
Wang WJ, Ling YY, Zhong YM et al (2022b) Ferroptosis-enhanced cancer immunity by a ferrocene-appended iridium(III) diphosphine complex. Angew Chem Int Ed 61(16):e202115247
Wang M, Wang Y, Mu Y et al (2023) Engineering SIRPα cellular membrane-based nanovesicles for combination immunotherapy. Nano Res 16(5):7355–7363
Xu C, Sun S, Johnson T et al (2021) The glutathione peroxidase Gpx4 prevents lipid peroxidation and ferroptosis to sustain Treg cell activation and suppression of antitumor immunity. Cell Rep 35(11):109235
Xue C, Zhang H, Wang X et al (2022a) Bio-inspired engineered ferritin-albumin nanocomplexes for targeted ferroptosis therapy. J Control Release 351:581–596
Xue T, Zhang Z, Fang T et al (2022b) Cellular vesicles expressing PD-1-blocking scFv reinvigorate T cell immunity against cancer. Nano Res 15:5295–5304
Yan Z, Wu S, Zhou Y et al (2022) Acid-responsive micelles releasing cinnamaldehyde enhance RSL3-induced ferroptosis in tumor cells. ACS Biomater Sci Eng 8(6):2508–2517
Yang WS, SriRamaratnam R, Welsch ME et al (2014) Regulation of ferroptotic cancer cell death by GPX4. Cell 156(1–2):317–331
Yang J, Mo J, Dai J et al (2021) Cetuximab promotes RSL3-induced ferroptosis by suppressing the Nrf2/HO-1 signalling pathway in KRAS mutant colorectal cancer. Cell Death Dis 12(11):1079
Yang J, Jia Z, Zhang J et al (2022) Metabolic intervention nanoparticles for triple-negative breast cancer therapy via overcoming FSP1-mediated ferroptosis resistance. Adv Healthc Mater 11(13):e2102799
Yang F, Xiao Y, Ding J-H et al (2023) Ferroptosis heterogeneity in triple-negative breast cancer reveals an innovative immunotherapy combination strategy. Cell Metab 35(1):84–100
Ye Z, Liu W, Zhuo Q et al (2020) Ferroptosis: final destination for cancer? Cell Prolif 53(3):e12761
Zhang X, Wang C, Wang J et al (2018) PD-1 Blockade cellular vesicles for cancer immunotherapy. Adv Mater 30(22):e1707112
Zhang X, Sui S, Wang L et al (2020) Inhibition of tumor propellant glutathione peroxidase 4 induces ferroptosis in cancer cells and enhances anticancer effect of cisplatin. J Cell Physiol 235(4):3425–3437
Zhang X, Ge H, Ma Y et al (2023) Engineered anti-cancer nanomedicine for synergistic ferroptosis-immunotherapy. Chem Eng J 455:140688
Zhao L, Zhou X, Xie F et al (2022) Ferroptosis in cancer and cancer immunotherapy. Cancer Commun (lond) 42(2):88–116
Zhao J, Chen Y, Xiong T et al (2023) Clustered cobalt nanodots initiate ferroptosis by upregulating heme oxygenase 1 for radiotherapy sensitization. Small 19(10):2206415
Zhou Z, Liang H, Yang R et al (2022) Glutathione depletion-induced activation of dimersomes for potentiating the ferroptosis and immunotherapy of "cold" tumor. Angew Chem Int Ed 61(22):e202202843

## Publisher's Note